Advanced Energy Materials

ADVANCED ENERGY MATERIALS
www.advenergymat.de

RESEARCH ARTICLE OPEN ACCESS

Selective Charge Extraction Allows Fast Photomultiplication and Imaging in Rigid and Ultra-Flexible SWIR Organic Photodiodes

Matilde Brunetta[1,2] | Zhuoran Qiao[3] | Davide Nodari[3] | Kosei Sasaki[4] | Francesco Furlan[3] | Martina Rimmele[3] | Hongki Kim[3] | Hongting Chen[4] | Yusaku Tagawa[4] | Adam Marsh[5] | Rushil Vasant[6] | Sang Do[6] | Xabier Rodríguez-Martínez[7] | Anirudh Sharma[5] | Christos L. Chochos[8] | Jaime Martin[7] | Martin Heeney[3,5] | Koen Vandewal[9] | Derya Baran[5] | Thuc-Quyen Nguyen[6] | Bob C. Schroeder[2] | Takao Someya[4] | Tomoyuki Yokota[4,10] | Nicola Gasparini[3]

[1]Department of Materials, Molecular Science Research Hub, Imperial College, London, UK | [2]Department of Chemistry, University College London, London, UK | [3]Department of Chemistry and Centre for Processable Electronics, Imperial College London, London, UK | [4]Department of Electrical Engineering and Information Systems, The University of Tokyo, Tokyo, Japan | [5]Division of Physical Sciences & Engineering (PSE), Chemistry Program, King Abdullah University of Science and Technology (KAUST), Thuwal, Saudi Arabia | [6]Center for Polymers and Organic Solids (CPOS), Department of Chemistry and Biochemistry, University of California at Santa Barbara, Santa Barbara, California, USA | [7]Universidade Da Coruña, Campus Industrial de Ferrol, CITENI, Ferrol, Spain | [8]Institute of Chemical Biology, National Hellenic Research Foundation (NHRF), Athens, Greece | [9]Institute for Materials Research (IMO-IMOMEC), Hasselt University, Diepenbeek, Belgium and IMEC Division, IMOMEC, Diepenbeek, Belgium | [10]Institute of Engineering Innovation, Graduate School of Engineering, The University of Tokyo, Tokyo, Japan

Correspondence: Nicola Gasparini (n.gasparini@imperial.ac.uk)

Received: 9 December 2025 | **Revised:** 4 February 2026 | **Accepted:** 4 February 2026

Keywords: biomedical sensor | flexible organic photodiode | IR detection | organic photodiode | photomultiplication | pulse oximeter | ultralow bandgap polymer

ABSTRACT

Expanding the absorption window of organic photodiodes (OPDs) over the 1000 nm benchmark is essential for bioimaging and medical applications. However, progressing into this wavelength range has proven to be a challenging task due to the scarcity of near-infrared (NIR) semiconducting polymers and small molecules with suitable energy alignment and processability. OPDs based on low-bandgap donor polymers generally present low responsivities and, therefore, low detectivities in the NIR. Photomultiplication (PM) has been introduced as a promising strategy to increase the external quantum efficiency (EQE) above unity. However, its application has been mainly limited to OPDs operating in the visible range and with response speeds within the millisecond range. In this work, we present PM-OPDs utilizing an equal donor (D):acceptor (A) ratio in the bulk heterojunction photoactive layer. This changes the common understanding of PM-OPDs, in which heavily unbalanced D:A ratios were needed to impose trap-assisted charge tunnelling injection at high reverse bias. Here, the NIR polymer TQ-3T was used with nonfullerene acceptor Y6. PM-OPDs with an EQE of above 1100% at 840 nm and 31% at 1100 nm at -10 V, and fast response times of 73 µs were achieved. We also demonstrate ultrathin (<3 µm) flexible PM-OPDs based on the TQ-3T:Y6 blend without any drop in performance compared to rigid samples with a stable dark current density after 1000 bending cycles. Finally, we demonstrate an application of the PM-OPD as a flexible and pulse oximeter and large-area image sensor for accurate vein recognition.

1 | Introduction

In recent years, photodiodes have established themselves as an essential component in everyday technology. Their range of applications spans optical communication [1], environmental monitoring, and most importantly, medical care and medical imaging [2, 3]. In the near-infrared (NIR) region, inorganic photodiodes based on InGaAs or germanium currently lead the optical sensor market because of their outstanding carrier mobility and stability [4, 5]. With the exception of few emerging quantum dots technologies [6–8], most inorganic materials present major drawbacks such as expensive fabrication processes and mechanical rigidity [9], making traditional PDs unsuitable for future generation applications such as bioelectronics and skin-grafted sensors [10, 11]. Organic photodiodes (OPDs) are a promising candidate to address the limitations of traditional photodiodes, by accommodating the fast-growing demand for lightweight and cost-effective sensors that can be scaled [12] and flexible [13, 14]. To maximize the light-to-current conversion, an organic photoactive layer typically comprises a bulk heterojunction (BHJ) of an electron-donor (D) and electron-acceptor (A) material. By adopting this device architecture, OPDs present notable advantages such as photon-to-charge carrier conversion yield approaching unity and solution processability, which allows deposition of the photoactive layer onto a selection of surfaces, and a tunable absorption [15, 16], spanning from broadband to detection windows as narrow as a few nanometers. All of these are key qualifications for wearable electronics, flexible imagers and on-the-go monitoring.

For biosensing [17] and imaging [18, 19] in particular, it is essential to assess two main factors: the OPD detection window and an enhanced responsivity at such wavelengths. The ideal detection window for a bioimaging sensor is in the NIR-II range (from 1100 to 1300 nm), to allow better tissue penetration, minimize light attenuation and improve contrast compared to visible light [20, 21]. However, the synthetic challenges of developing low-bandgap, solution-processable donor polymers [22–24] result in a scarcity of NIR materials with an absorption onset above the 1000 nm benchmark. Therefore, there is a limited amount of well-performing OPDs that operate in the NIR-I (800–1100 nm) and NIR-II range [25, 26]. In previous work, we reported two NIR OPDs based on thiadiazoloquinoxaline-thiophene (TQ-T) [27] and terthiophene (TQ-3T) [28] polymers with a non-fullerene acceptor (IEICO-4F) showing a photocurrent response up to 1800 nm and a moderately high specific detectivity (D^*) of 10^{10} Jones at 1200 nm (TQ-3T:IEICO-4F). The small bandgap for both donor polymers can be attributed to the strongly accepting TQ monomer, which combines electron-deficient thiadiazole and quinoxaline moieties. Electron withdrawing units mostly contribute to a low lying lowest unoccupied molecular orbital (LUMO) level, however, the open-shell ground state character of TQ encourage a quinoidal structure along the backbone affecting the highest occupied molecular orbital (HOMO) [29, 30]. This molecular design allows the readily tuning of the bandgap, and the TQ monomer favors the addition of solubilizing alkyl chains which improve polymer solubility. However, the shallow HOMO levels of these TQ-based polymers hinder the desired ohmic contact with current hole-transporting layers (HTLs), resulting in higher dark current density (J_d) values. Nonetheless, detectivity (D^*) can be still enhanced by increasing the external quantum efficiency (EQE), and therefore the responsivity (R).

The photomultiplication (PM) effect has emerged as a potential solution to enhance the photoresponse of an OPD without compromising its simple structure. In literature, OPDs are differentiated into photodiode-type OPDs with an EQE below 100% and PM-OPDs showing an EQE above 100% [31, 32], affirming that it is impossible to obtain PM OPDs with the same simple structure of a standard OPD [33]. As a result of such high EQEs, PM-OPDs have demonstrated state-of-the-art responsivities, with values exceeding 124 A W^{-1}, [34] albeit with the drawback of a higher dark current and longer response times on the order of milliseconds compared to the photodiode-type OPD counterpart [35, 36]. The working mechanism of PM OPDs entails trapping one of the photogenerated charge carriers in either the active layer or at an interfacial blocking layer. Such trapped charges lower the injection barrier for the opposite carriers, enabling tunnelling from the electrode and thereby generating a photocurrent gain in which several charges may be collected for each absorbed photon [37]. The PM effect can be obtained through several strategies, such as introducing further charge blocking layers into the OPDs architecture to enhance the charge injection at reverse bias [38, 39], or by incorporating quantum dots [40], as well as adding dopants [41]. So far, the most common strategy to achieve PM is introducing traps into the active layer by implementing a heavily unbalanced D:A ratio (e.g. 100:1 by weight) in the BHJ [42–45], such that one phase cannot form a continuous charge extraction pathway and therefore acts as a trap site. While useful for PM, such unbalanced D:A ratios exhibit an increase in charge recombination and consequently dark current values, as well as reducing response speeds [46].

In this work, we present a NIR-II PM OPD for biomedical sensing with a photoresponse up to 1450 nm, employing a balanced TQ-3T:Y6 (D:A) ratio of 1:1 and a simple device OPD architecture. The PM effect in an inverted configuration OPD was achieved by tuning the energy alignment of the donor polymer TQ-3T and hole blocking layer MoOx, as well as exploiting the electron and hole mobility mismatch between the non-fullerene acceptor (NFA) Y6 and TQ-3T. We discovered that the non-ohmic contact formed between MoOx and the HOMO of TQ-3T causes a selective charge accumulation of holes at the interface of the active layer, while allowing the extraction of tunnelling electrons through the LUMO of Y6. Additionally, TQ-3T acts as a trapping material because of its low hole mobility, resulting in an EQE of above 1100% in the visible range and of 31% at 1100 nm at -10 V. Sub-millisecond response times are retained with rise and fall times of 73 and 76 µs, respectively. To prove the viability of our PM-OPDs, we demonstrate ultrathin and flexible TQ-3T:Y6 PM OPDs with a highly stable dark current density over 1000 cycles of repeated bending stress. The flexible OPD was used as photoplethysmogram (PPG) sensor to record the heartbeat and calculate the blood saturation as a pulse oximeter. Finally, an application of TQ-3T:Y6 PM OPD as a large-area flexible active-matrix image sensor for vein authentication was reported. These unprecedented applications of a PM-OPD in ultrathin and flexible technologies, as well as in conformable skin sensors, uncovers yet unexplored research prospects regarding the photomultiplication effect in the biomedical field.

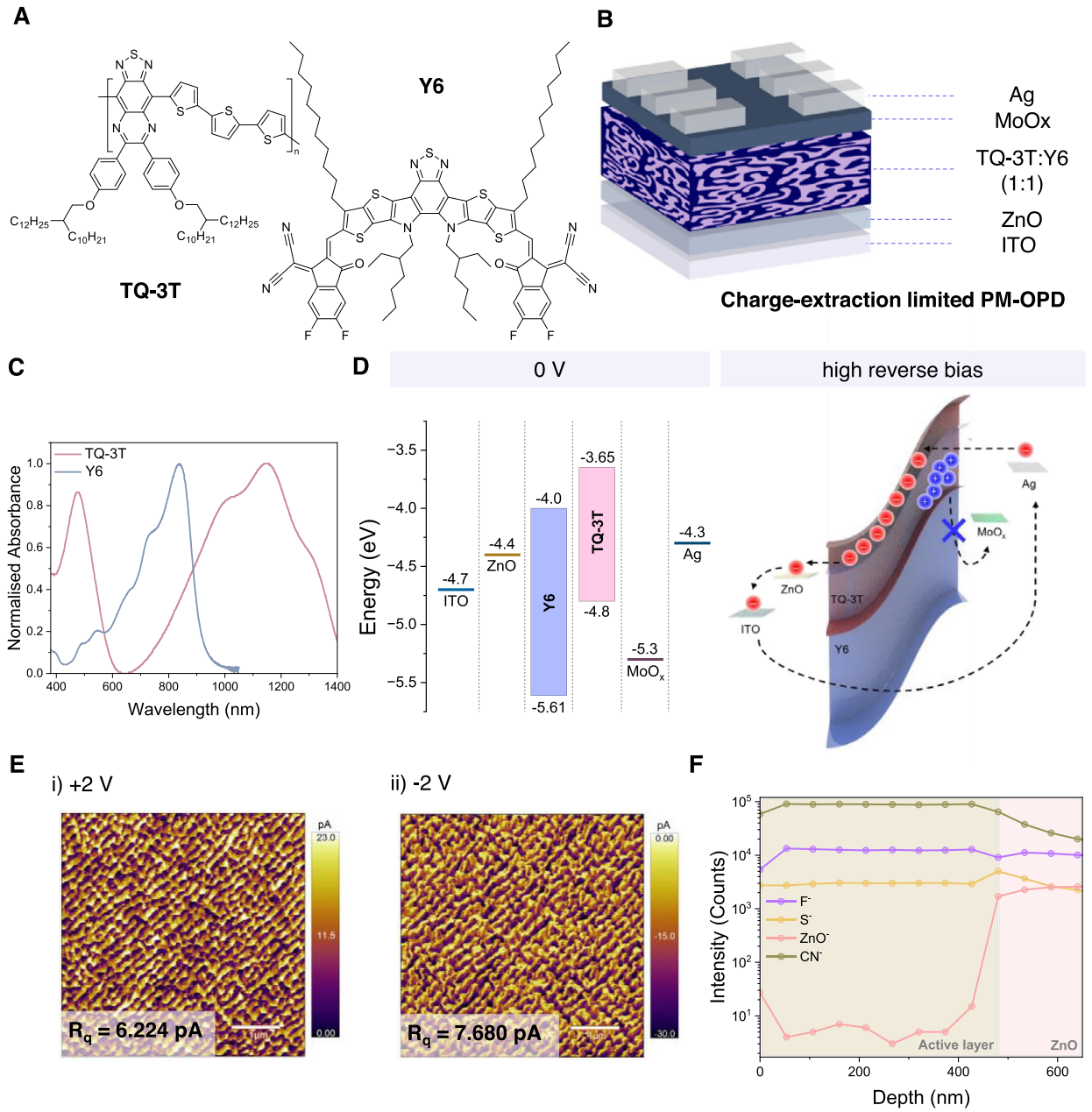

FIGURE 1 | OPD materials characterization. (a) Chemical structures of TQ-3T and non-fullerene acceptor Y6. (b) Schematic of a charge-extraction limited PM-OPD highlighting the adopted inverted architecture. (c) Normalized visible-IR absorption spectra of TQ-3T and Y6. (d) (left) Schematic showing the energy levels of the OPD materials. The ionization energy (IE) and electron affinity (EA) of Y6 and TQ-3T were measured using ultraviolet photoelectron spectroscopy (UPS) and low-energy inverse photoelectron spectroscopy (LE-IPES), respectively (Figures S2 and S3) [47, 48], and (right) schematic of the expected band-bending under high reverse bias. (e) C-AFM images of TQ-3T:Y6 1:1 (wt/wt) blend at (i) +2 V illustrating the hole collection network and at (ii) -2 V illustrating the electron collection network. (f) Time-of-flight secondary ion mass spectrometry (ToF-SIMS) depth profile of ITO/ZnO/TQ-3T:Y6 1:1 (wt/wt) sample.

2 | Results

2.1 | OPD Material Characterization

TQ-3T (Figure 1a) was synthesized (Figure S1) and blended in a bulk heterojunction with commercially available NFA Y6 in a 1:1 ratio (wt/wt). Figure 1b shows the device architecture of our charge-extraction limited PM-OPD and Figure 1c shows the normalized absorption spectra of the donor (D) and acceptor (A) material used in our PM-OPDs.

Conventionally, highly unbalanced D:A ratios (on the order of 100:1 to 100:16 [49]) are necessary to obtain PM in OPDs. The acceptor molecules, present in smaller quantities, act as a trap in the photoactive layer, hindering hole extraction. The trapped charges bend the energy levels, lowering the barrier for hole injection, such that under large reverse bias additional holes can tunnel into the active layer, leading to a large photocurrent gain. In contrast, in this work we used a balanced D:A (1:1, wt/wt) ratio in a bulk heterojunction to achieve PM, exploiting the inherent mobility imbalance between the two materials, and electron

tunnelling induced by charge accumulation at the TQ-3T/MoOx interface due to the large energy offset (Figure 1d).

BHJ films were prepared using a blade coating method in air as it allowed higher control over the active layer thickness as compared to the spin-coating method. 2D grazing-incidence wide-angle X-ray scattering (GIWAXS) and conductive atomic force microscopy (C-AFM) analysis provided complementary insights into the morphology and charge transport pathways of the photoactive layer. GIWAXS images (Figure S4) confirmed that TQ-3T preferentially adopts a face-on orientation in thin films and demonstrated that the deposition technique had no significant influence on the solid-state morphology or microstructure of the TQ-3T:Y6 blend. C-AFM further confirmed the homogeneity of current distribution across the BHJ, with Figure 1e showing the collection pathways under both forward (holes) and reverse biases (electrons). Topographic AFM imaging (Figure S5) of the TQ-3T:Y6 1:1 (wt/wt) blend at 0 V confirms the overall smoothness of the film.

Finally, time-of-flight secondary ion mass spectrometry (ToF-SIMS) was performed on TQ-3T:Y6 1:1 (wt/wt) (Figure 1f) to gain a better insight into vertical phase distribution of the BHJ. The results showed no evidence of phase stratification of either TQ-3T or Y6, proving that both components were homogeneously mixed without any preferential accumulation at the interfaces.

2.2 | PM-OPDs Device Fabrication and Characterization

Given the similar materials distribution and microstructure, we fabricated inverted architecture OPDs with TQ-3T:Y6 in ratios of 2:1, 1:1 and 1:2 (wt/wt). The OPD structure consisted of indium tin oxide (ITO)/ZnO (30 nm)/Active layer (700 nm)/MoO_x (10 nm)/Ag (100 nm). The photodetection ability of TQ-3T:Y6-based OPDs was evaluated by measuring current density-voltage (*J-V*) characteristics under both dark and one sun illumination (AM1.5G) conditions. The devices with D:A ratios of 2:1, 1:1, 1:2 (wt/wt) delivered a dark current density (J_d) of 1.3×10^{-4}, 2.7×10^{-4}, 1.2×10^{-3} A cm^{-2} at -2 V and a photocurrent (J_L) of 2.7×10^{-3}, 7.3×10^{-3}, 1.5×10^{-2} A cm^{-2} at -2 V under AM1.5G illumination (Figure 2a, Figure S6, and Table S1 for photovoltaic parameters), respectively. The relatively high dark currents are attributed to the ultralow bandgap of TQ-3T [28]. As the bandgap of the donor polymer gets smaller, thermal excitation of electrons into the LUMO and back injection of electrons from the electrodes becomes more likely, resulting in higher values of dark current density [46].

Besides dark current density, EQE and spectral responsivity (SR) are essential OPD figures of merit used to quantify the photon-to-electron ratio of the detector. SR is closely related to the EQE and can be calculated from the following equation.

$$\mathrm{SR}\ \left(\mathrm{AW}^{-1}\right) = \frac{I_{\mathrm{ph}}}{P_{\mathrm{in}}} = \mathrm{EQE}\frac{\lambda \mathrm{q}}{h\mathrm{c}} \tag{1}$$

where I_{ph} is the output photocurrent, P_{in} is the input optical power, c is the speed of light, h is the Planck's constant, and q is the elementary electric charge.

As shown in Figure 2b, the TQ-3T:Y6 OPD of 1:1 (wt/wt) D:A ratio showed an EQE spectra of 1129% at 840 nm, and specifically an EQE of 31% at 1100 nm in the NIR-II region at -10 V. Applying a higher reverse bias is necessary to allow effective charge extraction, this mechanism will be explained more in detail below. The calculated responsivity at -10 V was 7.6 A W^{-1} at 840 nm and 0.26 A W^{-1} at 1100 nm (Figure S7). TQ-3T:Y6 is the first reported OPD with a balanced D:A ratio to achieve PM effect without the introduction of dopants, additives, or blocking layers, into the device architecture. To understand the underlying mechanism of this effect in our OPDs, we fabricated devices with different structures, including varied electron transporting layers (ETL), hole transporting layers (HTL) (Figures S8–S10), and alternative acceptors (Figure S11 and Table S2). Our aim was to determine whether the PM effect originated from electron tunneling, with MoOx acting as a blocking layer due to its energy misalignment with TQ-3T. In our hypothesized scenario, the energetic mismatch would lead to hole accumulation at the donor polymer/MoOx interface, with these carriers remaining trapped even under the large band bending induced by reverse bias. On the other hand, MoOx does not block electrons which are able to tunnel through the LUMO of Y6 and be successfully extracted. Our second supposition was that TQ-3T acted as a trap in a BHJ with Y6 due to its low hole mobility (5.63×10^{-7} cm^2 V^{-1} s^{-1}) compared with the much higher electron mobility of Y6 (1.84×10^{-4} cm^2 V^{-1} s^{-1}), as determined by space charge limited current (SCLC) measurements (Figure S12). After a careful study (see Supporting Information), we were able to confirm that the PM effect occurred as a result of a synergetic contribution of both factors, proving the 1:1 (wt/wt) TQ-3T:Y6 offers the optimal trade-off between absorption and gain.

Specific detectivity (D^*), calculated with the equation below, is an essential parameter to assess the light-sensing applications of OPDs.

$$D^*\ (\mathrm{Jones}) = \frac{\mathrm{SR}\sqrt{A\Delta f}}{i_{\mathrm{n}}} \tag{2}$$

where A is the active area of the photodiode, Δf is the detection bandwidth and i_n is the noise current spectral density. Figure 2d shows both the calculated D^* from shot noise (dashed), which is directly linked to the J_d of the device, and the measured detectivity (solid) from measured noise spectral density (Figure 2c). The measured detectivity considers both the flicker noise and thermal noise which have a significant impact on the overall value of detectivity, explaining why the calculated detectivity usually results in an overestimation of the measured data [50]. TQ-3T:Y6 1:1 (wt/wt) delivered a measured specific detectivity of 1.5×10^{10} Jones at 840 nm and 5.1×10^8 Jones at 1100 nm at -10 V.

The current bottleneck for PM-OPDs to be competitive for optical communication and video applications is their slow response rate. PM-OPDs feature slow response speeds in the order of milliseconds, limited by both the photo-carrier lifetime and the time required for trap filling and band bending. In contrast, our balanced D:A BHJ utilized mobility imbalance and interfacial energetics. This allows PM effect without deep trapping, thereby retaining response times on the order of microseconds and allowing more efficient charge extraction. To confirm the suitability of our OPD in video and imaging applications, we examined

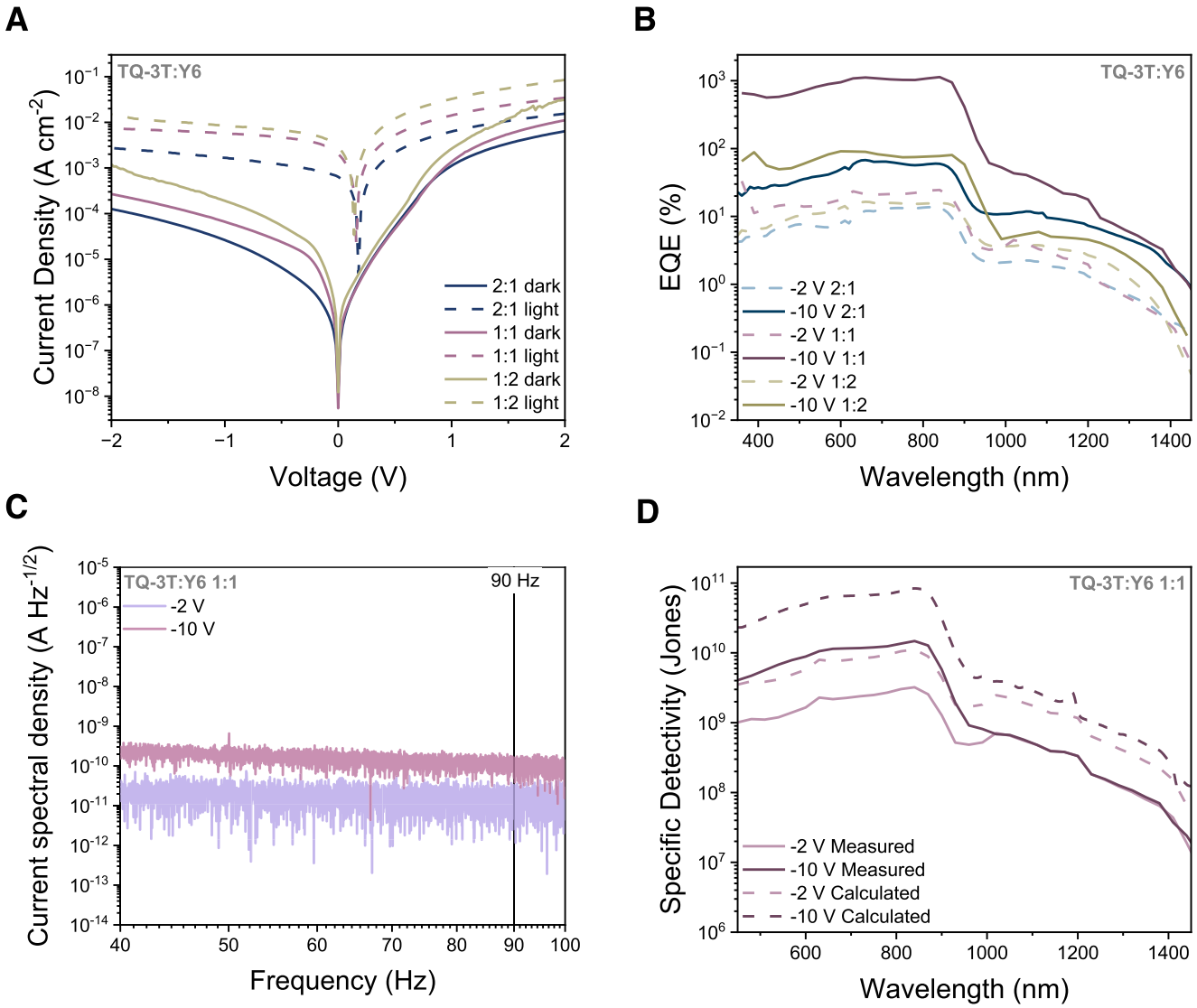

FIGURE 2 | Device characterization. (a) Current density–voltage characteristics of TQ-3T:Y6 (2:1, 1:1 and 1:2, wt/wt) OPDs under AM1.5G illumination and in dark conditions. (b) Bias-dependent EQE at -2 and -10 V for TQ-3T:Y6 2:1, 1:1, and 1:2 (wt/wt) OPDs. (c) Bias-dependent noise current spectral density of TQ-3T:Y6 1:1 (wt/wt) OPDs. (d) Shot-noise limited (dashed) and measured (solid) specific detectivity (D^*) of TQ-3T:Y6 1:1 (wt/wt).

the dynamic characteristics of TQ-3T:Y6. Figure 3a shows the response to IR illumination of 1100 nm under increasing reverse bias of TQ-3T:Y6 (1:1). Transient photocurrent measurement was key to understanding the mechanism of charge accumulation and extraction of the PM effect found in our OPDs. At low values of reverse bias (-2 V), charges accumulate and are not extracted, in line with EQE values below 100%. However, as reverse bias is increased, holes continue to accumulate at the donor interface, while electrons can successfully tunnel through the Y6 LUMO and be extracted more effectively, showing that the threshold bias to ignite the PM effect, and the associated band-bending, in our OPD is about -5 V (Figure 3d). Consequentially, the traces at -10 V are indistinguishable from the ones at -5 V. The rise t_r and fall t_f times of TQ-3T:Y6 2:1, 1:1, 1:2 (wt/wt) (Figure 3b) at -10 V under 1100 nm illumination are 218 and 299 µs, 73 and 76 µs, and finally 77 and 70 µs, respectively. Finally, for imaging applications OPDs should have a bandwidth greater than 10 kHz. The cut-off frequency refers to the frequency of an incident modulated light at which the photocurrent of the OPD is diminished by 3 dB of its original low-frequency value. The bandwidth of TQ-3T:Y6 1:1 (wt/wt) at -10 V under 1100 nm IR illumination was evaluated to be 43 kHz (Figure 3c), further demonstrating that our OPDs can be used for video applications. PM-OPDs with EQEs exceeding 1100% at 840 nm and response times in the order of microseconds are achieved, finally closing the gap in the PM field for real-world imaging and sensing technologies (Table S3).

2.3 | Ultra-Thin Flexible PM-OPDs and Conformable Large-Area Image Sensor

As a proof of concept, we implemented TQ-3T:Y6 in an ultrathin and flexible PM-OPD, to demonstrate the potential of this material for conformable biomedical monitoring. An OPD with same device architecture of Figure 1b was fabricated on an ultrathin parylene substrate (1 µm) (Figure 4a). Current density–voltage

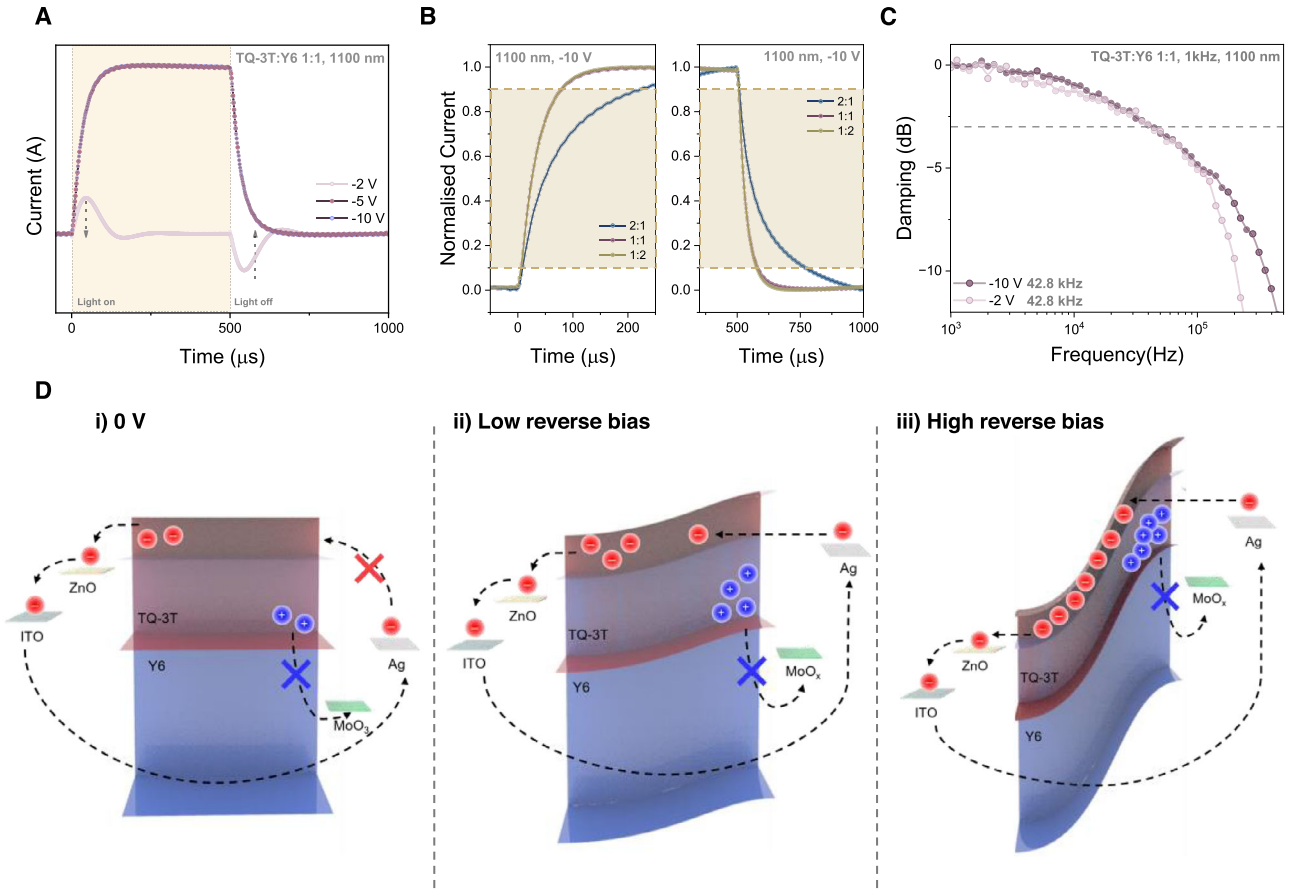

FIGURE 3 | OPD dynamic measurements and schematic diagram of PM effect. (a) Transient photocurrent measurements of TQ-3T:Y6 1:1 (wt/wt) at increasing reverse bias under 1100 nm illumination. (b) Transient photocurrent measurements with rise and fall times of TQ-3T:Y6 2:1, 1:1, and 1:2 (wt/wt) at -10 V under 1100 nm illumination. (c) Cut-off frequency at increasing reverse bias of TQ-3T:Y6 (1:1) under 1100 nm illumination with -3 dB damping. (d) Schematic of the bias-induced band bending (i) at no applied bias (0 V), (ii) at low reverse bias (-5 V) and finally (iii) at high reverse bias (-10 V) at which selective electron charge extraction and hole blocking is achieved.

characteristics in both light and dark conditions were evaluated (Figure S13) and were consistent with the OPDs devices based on glass even after removal from their temporary glass support. The stability of the dark current density was tested at different bending radii, spanning from 25 to 0.5 mm. *J–V* characteristics were found to be stable under bending stress with a 10% improvement of its original value at the 0.5 mm radius. The smallest radius of 0.5 mm was then selected to test the flexible stability of TQ-3T:Y6 over 1000 cycles in air (Figure 4b). Again, the dark current density of TQ-3T:Y6 remained stable over the increasing bending cycles, with a 15% improvement of its original value by the 1000th cycle. The suitability of the TQ-3T:Y6 blend into flexible OPDs can be attributed to the largely amorphous nature of TQ-3T as shown in the GIWAXS analysis, which indicates a disposition of the material to be docile to bending stress which is ideal in skin sensor applications. The superior stability of dark current density in our PM-OPDs was further proved by measuring the *J–V* characteristics of the device after storing it in air for 10 months. The performance showed a 1.49 fold increase compared to the freshly measured PM-OPDs at -2 V and a 2.71 fold increase at -10 V of dark current density (Figure S14).

As tissue penetration increases with wavelength, photoplethysmogram (PPG) measurements were recorded at three different wavelengths, 780, 940, and 1100 nm. When a fingertip is placed between the light source and the OPD, the volumetric changes in blood capillaries result in an altered transmittance to the NIR light, leading to a change of the photocurrent response of the OPD. Here, the PPG waveforms at increasing reverse bias (Figure S15) of a healthy volunteer in the fourth-decade age group were recorded, and the heartbeat was calculated to be of an average of 60 bpm. As expected, at -10 V, where band bending allows for PM, the PPG waveform is more clearly resolved compared to -2 V, allowing the systolic and diastolic peaks to be distinguished at all three wavelengths. This is consistent with the PM effect achieved at higher reverse bias. The acceleration plethysmogram (APG) (Figure 4c) is obtained through the second derivative of the PPG waveform and gives important insights into the cardiac cycle as well as arterial health. The APG signal at 1100 nm measured at -10 V is the only measurement that shows all four systolic waves, early systolic positive wave (a), early systolic negative wave (b), late systolic re-increasing wave (c), and the late systolic re-decreasing wave (d), as well as one diastolic wave, the early diastolic positive wave (e). The highly resolved peaks at 1100 nm are consistent with the deeper tissue penetration of SWIR light, and the enhanced photoresponse of our PM-OPD under increased reverse bias. The PPG waveform can also be used in pulse oximetry as an aid to extract the arterial oxygen saturation

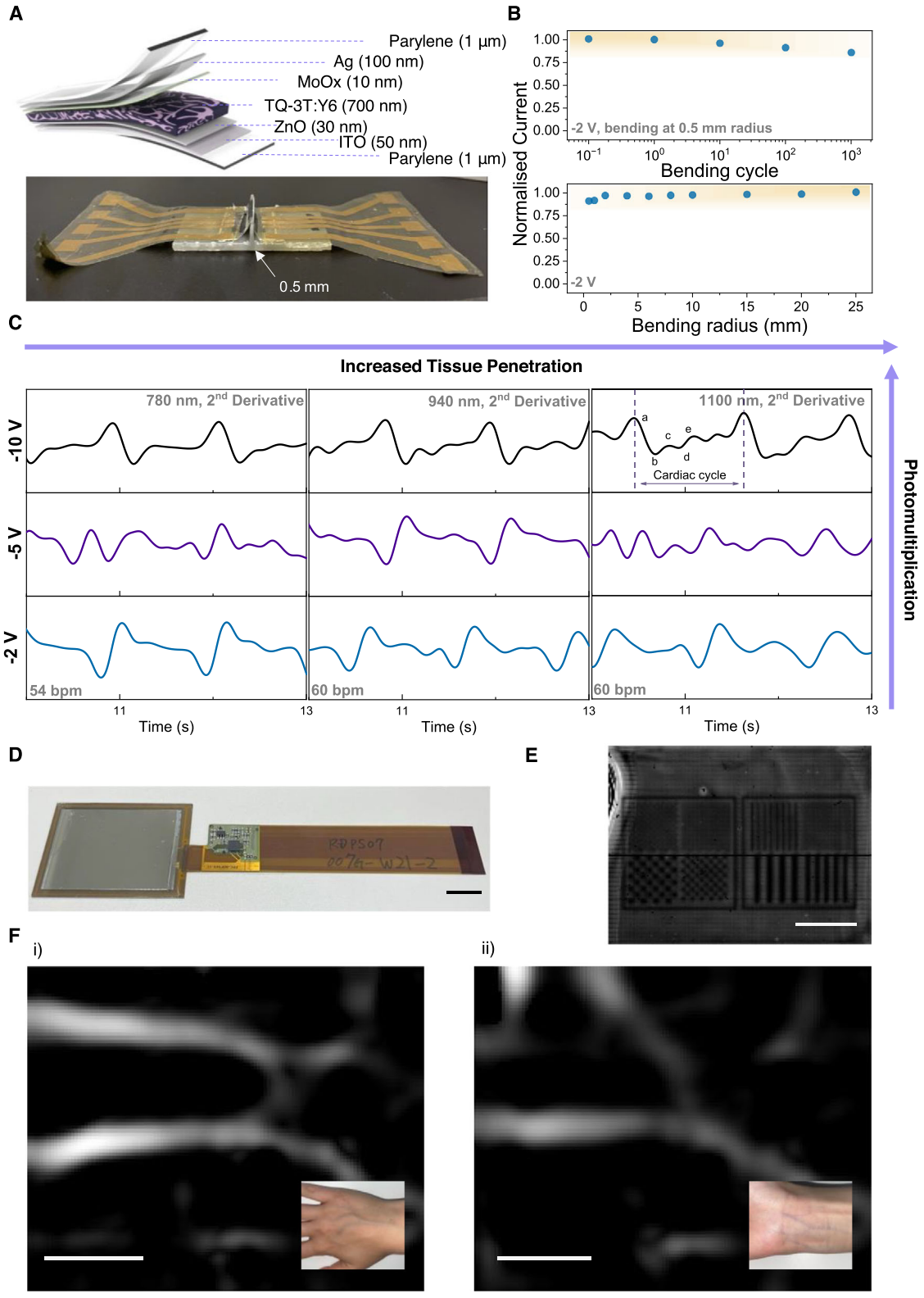

FIGURE 4 | Ultrathin flexible OPD for biometric monitoring and vein authentication. (a) (Top) Device architecture of our ultrathin flexible PM-OPD and (bottom) our ultrathin flexible PM-OPD detached from glass support showing full flexibility over the 0.5 mm radius structure. (b) (Bottom) Normalized dark current density of flexible OPD upon decreasing bending radii and (top) normalized dark current density of flexible OPD at 1, 10, 100 and 1000 bending cycles onto the 0.5 mm radius prop. (c) Bias-dependent APG signal at 780 nm, 940 nm and 1100 nm, highlighting the key elements of a cardiac cycle. (d) Image sensor fabricated onto the 126 × 168 LTPS TFTs flexible substrate. Scale bar, 1 cm. (e) Resolution chart of flexible image sensor. Scale bar, 1 cm. (f-i) Imaging of hand veins and (ii) imaging of wrist veins. Scale bar, 1 cm.

(SpO_2). The AC/DC ratio at different wavelengths is obtained by superimposing the pulsatile component AC onto the lower-frequency DC component [51]. The SpO_2 of 97% was calculated according to the equation below:

$$SpO_2 = \frac{\varepsilon_{\lambda_1,HB} - \varepsilon_{\lambda_2,HB} R}{\left(\varepsilon_{\lambda_1,HB} - \varepsilon_{\lambda_1,HB\,O_2}\right) + \left(\varepsilon_{\lambda_2,HB\,O_2} - \varepsilon_{\lambda_2,HB}\right) R} \quad (3)$$

where R is the ratio of AC to DC at two different wavelengths (in our case at 780 nm and 940 nm), εHbO_2 and εHb are the absorption coefficients of oxyhemoglobin and deoxyhemoglobin, extracted from [52].

Finally, a conformable flexible image sensor based on our TQ-3T:Y6 PM-OPD combined with a low-temperature polycrystalline silicon (LTPS)-based thin-film transistors (TFTs) backplane [53, 54] was developed. The imager had an active area of 3 cm × 4 cm with a total of 126 × 168 pixels, each pixel with a size of 235 µm (Figure 4d,e). Figure 4f-i,ii shows veins located in on the hand and the wrist of two different subjects. The conformable sensor resulted in a notably resolved image of both hand and wrist veins under 850 nm NIR light at 0 V. The imaged veins successfully show the key elements for vein authentication such as the vein branch point, branching angle and several veins.

3 | Conclusion

We demonstrated that blending TQ-3T and Y6 in a 1:1 (wt/wt) ratio yields OPDs with PM, achieving an EQE of over 1100% at -10 V. We believe that these findings broaden the general understanding of PM, showing it can be achieved without highly unbalanced D:A ratios and within a conventional architecture. The PM effect arises from a competition between the mobility imbalance of the two materials, TQ-3T and Y6, as well as the electrons tunnelling through Y6, while the HTL MoOx acts as a hole blocking layer considering its wide energy offset with TQ-3T. When sufficiently high reverse bias is applied, band bending is effectively achieved, allowing charges to be extracted. Our OPDs resulted in response times on the order of microseconds, amongst the fastest reported for PM-OPDs, confirming the suitability of our OPDs in imaging and sensing applications. Given the largely amorphous nature of TQ-3T, we fabricated flexible PM-OPDs with a highly stable dark current density upon bending, demonstrating how TQ-3T:Y6 can be used for conformable biometric applications. Accurate heartbeat measurements in PM mode with highly resolved cardiac cycle features were recorded. An application of our PM-OPD as a flexible pulse oximeter was also demonstrated. Finally, we have developed a, flexible active-matrix image sensor based on a 126 × 168 LTPS TFTs. Our flexible and conformable imager could capture detailed images of both hand veins and wrist veins, establishing TQ-3T:Y6 as a promising material combination for vein authentication. This application marks a significant advancement in wearable biometric imaging systems enabled by a new PM mechanism based on selective charge extraction that was established in our work.

4 | Methods

4.1 | Materials

TQ-3T was synthesized following the procedure by Jacoutot et al. [28]. Y6 was purchased from Ossila.

4.2 | Ultraviolet–Visible Spectroscopy (UV–Vis) Measurement

The UV–Vis measurement was carried out using SHIMADZU UV-2600i from 400 to 1400 nm with medium scan speed. UV–Vis samples were prepared by spin coating organic materials onto glass substrates with additional thermal annealing treatment. The absorption background of glass substrate was extracted before measurement.

4.3 | Ultraviolet Photoelectron Spectroscopy (UPS) and Low-Energy Inverse Photoelectron Spectroscopy (LE-IPES)

UPS and LE-IPES measurements were performed on thin films of TQ-3T (deposited on clean ITO using $ChCl_3$). UPS measurements were performed in an ultrahigh-vacuum chamber (base pressure, 10^{-10} mbar) using an ARGUS-CU analyzer equipped with a 128-channel stripped anode detector (Scienta Omicron), calibrated against the Fermi edge of clean polycrystalline silver. UPS measurements were conducted using a low-intensity UV light source (He I) with an excitation energy of 21.22 eV and a pass energy of 2 eV.

LE-IPES measurements were performed in isochromatic mode utilizing a home-built ultra-high vacuum setup, operational at a base pressure of 10^{-9} mbar. Photons emitted were captured using a solid-state photomultiplier tube (PMT) detector (Hamamatsu R585), positioned external to the vacuum. The detector was equipped with a Semrock 280 nm bandpass filter, which allowed a narrow wavelength window of 10 nm, with an integration time of 10 s to a maximum of 15 s. UPS measurements were first performed, and samples were then transferred from the UPS to the LE-IPES manipulator within the controlled ultra-high vacuum environment, without ambient air exposure. IE and EA of Y6 were determined on thin films deposited from a $ChCl_3$ solution, on Au-coated Si substrates, as reported earlier. The UPS and LE-IPES spectra were fitted with Gaussian peaks and a Tougaard background for determining the onset energies. Reproducibility of IE and EA values determined using UPS and LE-IPES is ± 0.05 eV and ± 0.1 eV, respectively [47, 48].

4.4 | Conductive Atomic Force Microscopy (C-AFM)

The C-AFM measurements were carried out in a nitrogen-filled glove box using an MFP-3D system (Asylum Research) mounted on an Olympus inverted optical microscope with a

Xenon lamp illumination source (Newport Oriel Instruments). Gold/chromium-coated silicon conductive AFM probes with a resonant frequency of 20 kHz and a spring constant of 0.3 N m^{-1} (MikroMasch) were used to acquire all C-AFM and AFM surface images. The setup allows for the simultaneous measurement of nanoscale current and surface topography mapping in contact mode.

4.5 | Time-of-Flight Secondary Ion Mass Spectrometry (ToF-SIMS) Measurement

ToF-SIMS measurements were conducted on ITO/ZnO/TQ-3T:Y6 1:1 (wt/wt) sample. The samples were depth profiled using an IONTOF ToF-SIMS V instrument. A 25 keV Bi^{+}_{3} ion beam in HCBM was used to analyze the sample, over a 150 × 150 μm^2 area with 128 × 128 pules. The samples were sputtered using a 10 keV $Ar_{15000}{}^{+}$ GCIB over an area of 500 × 500 μm^2. Final sputter crater depths were measured using the Zygo NexView optical interferometer.

4.6 | Grazing Incidence Wide-Angle X-Ray Scattering (GIWAXS) Measurement

GIWAXS measurements were performed at the non-crystalline diffraction beamline (BL11-NCD-SWEET) at ALBA Synchrotron Radiation Facility in Spain. The incident X-ray beam energy was set to 12.4 keV and the angle of incidence set at 0.12°. A detector (Rayonix LX255-HS) with a resolution of 1920 × 5760 pixels was used to collect the scattered patterns. The data was calibrated using Cr_2O_3 as standard (NIST) resulting in a sample-to-detector distance of 204.84 mm. The exposure time was set to 1 s.

4.7 | Organic Photodiodes (OPDs) Fabrication

Organic photodiodes were fabricated in a cleanroom environment using an inverted structure (glass/ITO/ZnO/active layer/MoO_x/Ag). Indium tin oxide (ITO, 15 Ω sq^{-1}) was pre-patterned on 12 mm × 12 mm glass substrates. The substrates underwent a cleaning process involving sonication in acetone for 10 min, followed by detergent and deionized water. After an additional 10-minute sonication in acetone, the substrates were cleaned with isopropanol and immediately subjected to an 8-minute UV-ozone treatment.

A 40 nm thick ZnO layer was deposited on the ITO through spin-coating at 4000 rpm for 40 s, using a zinc acetate dihydrate precursor solution. The coated substrates underwent thermal annealing (TA) treatment at 180°C for 10 min. The active layer solution, comprising a blend of donor (TQ-3T) and acceptor (Y6) in chloroform, was prepared in a 1:1, 2:1 and 1:2 ratio (wt/wt) at a concentration of 30 mg mL^{-1}. The solutions were stirred overnight in the glove box at room temperature and heated to 50°C for 2 h before blade-coating to ensure complete dissolution.

The active layer solutions were doctor blade-coated onto the ZnO from the warm solution in air, at a speed of 70 mm s^{-1}. The resulting active layers underwent TA treatment on a programmable heat plate in a N_2-filled glove box at 100°C for 10 min. For thermal evaporation, a 10 nm MoO_x layer followed by a 100 nm Ag layer were sequentially deposited. The MoO_x layer was deposited at a rate of 0.15 Å s^{-1}, and the Ag layer deposition speed ranged from 0.5 to 1 Å s^{-1}. Each pixel's area, defined by a shadow mask, was 0.048 cm^2.

4.8 | Organic Photodiodes (OPDs) Characterization

J–V measurements were conducted using a Keithley 4200 Source-Measure unit (scan rate 25 mV s^{-1}). An Oriel Instruments Solar Simulator with a Xenon lamp and calibrated to a silicon reference cell was used to provide AM1.5G irradiance.

Responsivity was measured using an integrated system from Quantum Design PV300 with a modulation frequency of 90 Hz. All the devices were tested in ambient air.

Dynamic measurements were performed using a digital oscilloscope (Siglent, SDS6054A). The OPDs were illuminated with an 880 nm and 1100 nm LED driven by a function generator (ThorLabs DC2200). For the determination of the rise and fall time, a 1 kHz square wave pulse was applied to the LED using the function generator. For the determination of the cut-off frequency, sinusoidal functions with a frequency of 1 kHz were used to drive the LED connected to a digital oscilloscope (Siglent, SDS6054A). All the devices were tested in ambient air at room temperature.

4.9 | Noise Spectral Density Measurement

The devices were connected to a Zurich MFLI 500 and to a Keithley 2400. A bias of -2 and -10 V was applied with the Keithley 2400, while the dark current signal over time was recorded with the lock-in using an effective bandwidth of 172 Hz. The noise spectral density spectra have been obtained by conducting the Fast Fourier Transform (FFT) of the dark current over time. The measurement was conducted in ambient air at room temperature.

4.10 | Charge Carrier Mobility Measurement

The mobility of each pristine material and blends was measured using steady-state space-charge limited current (SCLC) method. To make sure device electrodes can inject the desired charge carrier while blocking the carrier with different polarity, hole-only (glass/ITO/active layer/MoOx/Ag) and electron-only (glass/ITO/ZnO/active layer/Ca/Al) devices were fabricated. Devices were placed in the sample chamber and then measured in the dark from 0 to 10 V under nitrogen environment.

4.11 | Flexible Organic Photodiodes (OPDs) Fabrication

The flexible OPDs were fabricated following a similar process reported by Wijaya et al. [55] onto a 1-μm parylene and a 500-nm

SU-8 epoxy layer. First, the supporting glass substrate was cleaned by immersing it in a degreasing agent (Furuuchi Chemical, Semicoclean 56) and ultrasonicating it at 45°C for 5 min. The glass was then repeatedly rinsed by immersing it in ultrapure water for 30 s and ultrasonicating it again at 45°C for 5 min. Finally, it was treated with Ar plasma ashing at 300 W for 5 min. The glass substrate was then spin-coated with a fluorinated polymer (a mix of 3 M Novec 1700 and Novec 7100, in a volume ratio of 1:6) at 2000 rpm for 30 s. Next, parylene (Daisan Kasei, diX-SR, 2 g) was deposited via chemical vapor deposition. The deposited parylene was annealed at 180°C for 30 min in a glovebox. Subsequently, a layer of epoxy (MicroChem, SU-8 3005) was spin-coated at 5000 rpm for 60 s to form a 500-nm-thick planarization layer. The epoxy film was exposed to ultraviolet light, annealed at 95°C for 3 min and at 180°C for 30 min. The active layer was blade-coated on top of ZnO thin film. 10 nm of MoO_x and 100 nm of Ag were thermally deposited. Contacts of the ultrathin OPDs were electrically connected with thin Au wiring on a 12.5 μm polyimide film using anisotropic conductive film (3 M, ECATT 9703) tapes as extended contact parts.

4.12 | Flexible Imager Fabrication

The flexible image sensor is fabricated following the similar process reported by Yokota et al. [2] and Wang et al. [54]. First, the LTPS TFT backplane is fabricated on a polyimide substrate. Each pixel consists of an n-type metal-oxide-semiconductor (NMOS) TFT with a double-gate structure. And the gate driver is formed by CMOS circuits using both p-type MOS and NMOS TFTs. A planar layer is deposited on the TFT backplane, followed with the OPD layer formed on top. The active layer was blade-coated on top of ZnO thin film. 10 nm of MoO_x and 100 nm of Ag were thermally deposited. Last, an encapsulation layer of 1.5 μm of parylene is further formed via chemical vapor deposition.

4.13 | Image Sensor Signal Recording and Postprocessing of Veins Images

This device has a one-transistor-one-capacitor structure, and the image is read in progressive scan mode. The sampling timing is 18 ms, and a sampling rate of 55.6 Hz. The flexible image sensor uses a special readout system to store the raw 10-bit image signal from the analog-to-digital converter to the computer. The vein was observed using transmitted light. View control film (Shin-Etsu Polymer Co., N-VCF1003000-PC100-X) was used as a flexible louvre to transmit only the vertical component of the light transmitted from the hand or wrist. The vein was imaged using all sensors (126 × 168) under an LED with a wavelength of 850 nm (NISSIN ELECTRONIC CO., LTD., IRTE-3041).

The raw image sensor's data were post-processed through a series of three to four steps. First, vertical stripe artifacts were removed by subtracting the average intensity across the 168-pixel width from each frame. Second, contrast was enhanced using contrast-limited adaptive histogram equalization (CLAHE) [56]. Third, Frangi filtering [57] was applied to enhance vein structures. Finally, binary segmentation of veins and surrounding tissues was performed using either global [58] or local Otsu thresholding [59]. (Main figures display images processed up to the third step).

Author Contributions

M.B. planned the research and designed the experiments under the guidance of N.G and B.C.S. M.B. synthesized the materials under the supervision of M.R. A.M. performed GPC analysis. X.R.-M. and J.M. performed the GIWAXS measurements. R.V. and S.D. performed C-AFM under the supervision of T.Q.N. A.S. and D.B. conducted UPS analysis and LE-IPES measurements and analysis. M.B. fabricated and optimized OPDs and carried out the device characterizations. M.B. and D.N. performed noise spectral density of OPD devices. F.F. carried out SCLC data analysis. M.B., K.V., and N.G. modeled the extraction mechanism. M.B. and K.S. fabricated the flexible OPDs and tested the flexible stability under the supervision of T.Y. and T.S. Z.Q. carried out device characterization of flexible OPDs. M.B. fabricated the active-matrix flexible imager. M.B. and H.C. conducted the imager application verification and Y.T. carried out the data analysis. M.B. wrote the initial draft of the manuscript under the supervision of N.G. All authors contributed to the work and commented on the paper.

Acknowledgements

N.G. and M.H. thank the King Abdullah University of Science and Technology (KAUST) Office of Sponsored Research (OSR) under Award ORFS-2023-OFP-5544. M.B. and N.G. thank the EPSRC Centre for Doctoral Training in the Advanced Characterisation of Materials (grant number EP/L015277/1). M.R. and N.G. would like to thank the EU Horizon project ENLIGHTENED (101172797) for funding. R.V. acknowledges financial support from the NSF Division of Chemistry (2404409). S.D. acknowledges financial support from the Mitsubishi Chemical Center for Advanced Materials (MC-CAM). B.C.S. acknowledge funding from the UK Research and Innovation for Future Leaders Fellowship (MR/Y003802/1). A.S. and D.B. thank the KAUST Solar Platform (KSP) for granting access to the characterization and device fabrication facilities and equipment employed herein. GIWAXS experiments were performed at NCD-SWEET beamline at ALBA Synchrotron with the collaboration of ALBA staff (experiment ID 2024098865). This work was supported by JSPS KAKENHI (Grant No. JP23H00173), JST ASPIRE for Rising Scientists (JPMJAP2336).

Funding

Japan Science and Technology Corporation JPMJAP2336; Division of Materials Research 2404409; Horizon 2020 Framework Programme 101172797; Engineering and Physical Sciences Research Council, MR/Y003802/1; Global Collaborative Research, King Abdullah University of Science and Technology ORFS-2023-OFP-5544.

Conflicts of Interest

The authors declare no conflicts of interest.

Data Availability Statement

Data are available from the corresponding authors upon reasonable request.

References

1. M. Babics, H. Bristow, W. Zhang, et al., "Non-Fullerene-Based Organic Photodetectors for Infrared Communication," *Journal of Materials Chemistry C* 9 (2021): 2375–2380, https://doi.org/10.1039/D0TC05341D.

2. T. Yokota, T. Nakamura, H. Kato, et al., "A Conformable Imager for Biometric Authentication and Vital Sign Measurement," *Nature Electronics* 3 (2020): 113–121, https://doi.org/10.1038/s41928-019-0354-7.

3. S. Liu, X. Zhang, X. Gu, and D. Ming, "Photodetectors Based on Two Dimensional Materials for Biomedical Application," *Biosensors and Bioelectronics* 143 (2019): 111617, https://doi.org/10.1016/j.bios.2019.111617.

4. Z. Zhao, C. Xu, L. Niu, X. Zhang, and F. Zhang, "Recent Progress on Broadband Organic Photodetectors and Their Applications," *Laser & Photonics Reviews* 14 (2020): 2000262, https://doi.org/10.1002/lpor.202000262.

5. A. Rogalski, "Infrared Detectors: An Overview," *Infrared Physics & Technology* 43 (2002): 187–210, https://doi.org/10.1016/S1350-4495(02)00140-8.

6. X. Tang, Y. Jiang, Z. Duan, et al., "Surface Ligand Engineering of Ag_2Te Colloidal Quantum Dots for a Self-Powered Shortwave Infrared Photodetector," *Journal of Materials Chemistry C* 13 (2025): 21418–21427, https://doi.org/10.1039/D5TC02959G.

7. W. Zeng, Z. Duan, Y. Bu, et al., "A Self-Powered HgTe Quantum Dots/PBDB-T:Y6 Bipolar Broadband Photodetector for Logic Gates," *Materials Horizons* 12 (2025): 2179–2186.

8. Y. Bu, Y. Jiang, Z. Duan, et al., "Oriented Crystallization of HgTe Quantum Dots with Low Urbach Band-Tail for Broadband Optoelectronic Logic Gates," *Advanced Optical Materials* 13 (2025): 2500295, https://doi.org/10.1002/adom.202500295.

9. D.-M. Geum, S. K. Kim, S. Lee, et al., "Monolithic 3D Integration of InGaAs Photodetectors on Si MOSFETs Using Sequential Fabrication Process," *IEEE Electron Device Letters* 41 (2020): 433–436, https://doi.org/10.1109/LED.2020.2966986.

10. H. Jinno, T. Yokota, M. Koizumi, et al., "Self-Powered Ultraflexible Photonic Skin for Continuous Bio-Signal Detection via Air-Operation-Stable Polymer Light-Emitting Diodes," *Nature Communications* 12 (2021): 2234.

11. L. Sun, J. Wang, H. Matsui, et al., "All-Solution-Processed Ultraflexible Wearable Sensor Enabled with Universal Trilayer Structure for Organic Optoelectronic Devices," *Science Advances* 10 (2024), eadk9460, https://doi.org/10.1126/sciadv.adk9460.

12. Y. S. Lau, Z. Lan, L. Cai, and F. Zhu, "High-Performance Solution-Processed Large-Area Transparent Self-Powered Organic Near-Infrared Photodetectors, " *Materials Today Energy* 21 (2021): 100708.

13. S. E. Root, S. Savagatrup, A. D. Printz, D. Rodriquez, and D. J. Lipomi, "Mechanical Properties of Organic Semiconductors for Stretchable, Highly Flexible, and Mechanically Robust Electronics," *Chemical Reviews* 117 (2017): 6467–6499, https://doi.org/10.1021/acs.chemrev.7b00003.

14. H. Ren, J. Chen, Y. Li, and J. Tang, "Recent Progress in Organic Photodetectors and Their Applications," *Advanced Science* 8 (2021): 2002418, https://doi.org/10.1002/advs.202002418.

15. J. Huang, H. M. Luong, J. Lee, et al., "Green-Solvent-Processed High-Performance Broadband Organic Photodetectors," *ACS Applied Materials & Interfaces* 15 (2023): 37748–37755, https://doi.org/10.1021/acsami.3c09391.

16. B. Xie, R. Xie, K. Zhang, et al., "Self-Filtering Narrowband High Performance Organic Photodetectors Enabled by Manipulating Localized Frenkel Exciton Dissociation," *Nature Communications* 11 (2020): 2871, https://doi.org/10.1038/s41467-020-16675-x.

17. M. Fu, Y. Chen, Y. Cao, et al., "Self-Filtering Narrowband Organic Photodetectors for Non-Invasive Blood-Oxygen Monitoring," *IEEE Electron Device Letters* 45 (2024): 1891–1894, https://doi.org/10.1109/LED.2024.3447588.

18. H. Park, Y. Dan, K. Seo, et al., "Filter-Free Image Sensor Pixels Comprising Silicon Nanowires with Selective Color Absorption," *Nano Letters* 14 (2014): 1804–1809, https://doi.org/10.1021/nl404379w.

19. S. Nishiwaki, T. Nakamura, M. Hiramoto, T. Fujii, and M. Suzuki, "Efficient Colour Splitters for High-Pixel-Density Image Sensors," *Nature Photonics* 7 (2013): 240–246, https://doi.org/10.1038/nphoton.2012.345.

20. L. A. Sordillo, Y. Pu, S. Pratavieira, Y. Budansky, and R. R. Alfano, "Deep Optical Imaging of Tissue Using the Second and Third Near-Infrared Spectral Windows," *Journal of Biomedical Optics* 19 (2014): 056004, https://doi.org/10.1117/1.JBO.19.5.056004.

21. E. Hemmer, A. Benayas, F. Légaré, and F. Vetrone, "Exploiting the Biological Windows: Current Perspectives on Fluorescent Bioprobes Emitting above 1000 nm," *Nanoscale Horizons* 1 (2016): 168–184, https://doi.org/10.1039/C5NH00073D.

22. X. Cao, J. Tong, Z. He, et al., "An Extremely Narrow Band Gap Conjugated Polymer for Photovoltaic Devices Covering UV to Near-Infrared Light," *Dyes and Pigments* 158 (2018): 319–325, https://doi.org/10.1016/j.dyepig.2018.05.052.

23. K. Wang, J. Huang, J. Ko, W. L. Leong, and M. Wang, "Direct Arylation Polymerization toward Ultra-Low Bandgap Poly(thienoisoindigo- alt -diketopyrrolepyrrole) Conjugated Polymers: the Effect of β-Protection on the Polymerization and Properties of the Polymers," *Journal of Polymer Science Part A: Polymer Chemistry* 55 (2017): 3205–3213, https://doi.org/10.1002/pola.28658.

24. J. Fan, J. D. Yuen, M. Wang, et al., "High-Performance Ambipolar Transistors and Inverters from an Ultralow Bandgap Polymer," *Advanced Materials* 24 (2012): 2186–2190, https://doi.org/10.1002/adma.201103836.

25. F. Verstraeten, S. Gielen, P. Verstappen, et al., "Efficient and Readily Tuneable Near-Infrared Photodetection up to 1500 nm Enabled by Thiadiazoloquinoxaline-Based Push–Pull Type Conjugated Polymers," *Journal of Materials Chemistry C* 8 (2020): 10098–10103, https://doi.org/10.1039/D0TC01435D.

26. Q. Li, Y. Guo, and Y. Liu, "Exploration of Near-Infrared Organic Photodetectors," *Chemistry of Materials* 31 (2019): 6359–6379, https://doi.org/10.1021/acs.chemmater.9b00966.

27. P. Jacoutot, A. D. Scaccabarozzi, T. Zhang, et al., "Infrared Organic Photodetectors Employing Ultralow Bandgap Polymer and Non-Fullerene Acceptors for Biometric Monitoring," *Small* 18 (2022): 2200580, https://doi.org/10.1002/smll.202200580.

28. P. Jacoutot, A. D. Scaccabarozzi, D. Nodari, et al., "Enhanced sub-1 eV Detection in Organic Photodetectors through Tuning Polymer Energetics and Microstructure," *Science Advances* 9 (2023), eadh2694, https://doi.org/10.1126/sciadv.adh2694.

29. Y. Joo, L. Huang, N. Eedugurala, et al., "Thermoelectric Performance of an Open-Shell Donor–Acceptor Conjugated Polymer Doped with a Radical-Containing Small Molecule," *Macromolecules* 51 (2018): 3886–3894, https://doi.org/10.1021/acs.macromol.8b00582.

30. L. Huang, N. Eedugurala, A. Benasco, et al., "Open-Shell Donor–Acceptor Conjugated Polymers with High Electrical Conductivity," *Advanced Functional Materials* 30, no. 24 (2020): 1909805, https://doi.org/10.1002/adfm.201909805.

31. J. Kim, M. Kang, S. Lee, C. So, and D. S. Chung, "Interfacial Electrostatic-Interaction-Enhanced Photomultiplication for Ultra-high External Quantum Efficiency of Organic Photodiodes," *Advanced Materials* 33, no. 52 (2021): 2104689, https://doi.org/10.1002/adma.202104689.

32. L. Li, F. Zhang, W. Wang, et al., "Trap-Assisted Photomultiplication Polymer Photodetectors Obtaining an External Quantum Efficiency of 37 500%," *ACS Applied Materials & Interfaces* 7 (2015): 5890–5897, https://doi.org/10.1021/acsami.5b00041.

33. Z. Li, Y. Yang, Y. Wu, et al., "Recent Progress on Photomultiplication Type Organic Photodetectors," *Journal of Physics D: Applied Physics* 58 (2025): 073004, https://doi.org/10.1088/1361-6463/ad983d.

34. D. Guo, D. Yang, J. Zhao, A. Vadim, and D. Ma, "Role of Interfaces in Controlling Charge Accumulation and Injection in the Photodetection Performance of Photomultiplication-Type Organic Photodetectors," *Journal of Materials Chemistry C* 8 (2020): 9024–9031, https://doi.org/10.1039/D0TC01590C.

35. J. Miao and F. Zhang, "Recent Progress on Photomultiplication Type Organic Photodetectors," *Laser & Photonics Reviews* 13 (2019): 1800204, https://doi.org/10.1002/lpor.201800204.

36. J. Miao, F. Zhang, M. Du, W. Wang, and Y. Fang, "Photomultiplication Type Organic Photodetectors with Broadband and Narrowband Response Ability," *Advanced Optical Materials* 6 (2018): 1800001, https://doi.org/10.1002/adom.201800001.

37. Y. Wang, S. Li, Y. Huang, et al., "Photomultiplication-Type Organic Photodetectors: Mechanisms, Integration toward Next-Generation Sensing Platforms," *Advanced Functional Materials* (2025): e18958, https://doi.org/10.1002/adfm.202518958.

38. N. Li, J. Lim, J. D. Azoulay, and T. N. Ng, "Tuning the Charge Blocking Layer to Enhance Photomultiplication in Organic Shortwave Infrared Photodetectors," *Journal of Materials Chemistry C* 8 (2020): 15142–15149, https://doi.org/10.1039/D0TC03013A.

39. D. Guo, D. Yang, J. Zhao, A. Vadim, and D. Ma, "Role of Interfaces in Controlling Charge Accumulation and Injection in the Photodetection Performance of Photomultiplication-Type Organic Photodetectors," *Journal of Materials Chemistry C* 8 (2020): 9024–9031, https://doi.org/10.1039/D0TC01590C.

40. R. Dong, C. Bi, Q. Dong, et al., "An Ultraviolet-to-NIR Broad Spectral Nanocomposite Photodetector with Gain," *Advanced Optical Materials* 2 (2014): 549–554, https://doi.org/10.1002/adom.201400023.

41. J. Huang, J. Lee, M. Schrock, et al., "Large-Gain Low-Voltage and Wideband Organic Photodetectors via Unbalanced Charge Transport," *Materials Horizons* 7 (2020): 3234–3241, https://doi.org/10.1039/D0MH01445A.

42. L. Shen, Y. Zhang, Y. Bai, X. Zheng, Q. Wang, and J. Huang, "A Filterless, Visible-Blind, Narrow-Band, and Near-Infrared Photodetector with a Gain," *Nanoscale* 8 (2016): 12990–12997, https://doi.org/10.1039/C6NR02902G.

43. H.-Y. Chen, M. K. F. Lo, G. Yang, H. G. Monbouquette, and Y. Yang, "Nanoparticle-Assisted High Photoconductive Gain in Composites of Polymer and Fullerene," *Nature Nanotechnology* 3 (2008): 543–547, https://doi.org/10.1038/nnano.2008.206.

44. Z. Zhao, C. Li, L. Shen, X. Zhang, and F. Zhang, "Photomultiplication Type Organic Photodetectors Based on Electron Tunneling Injection," *Nanoscale* 12 (2020): 1091–1099, https://doi.org/10.1039/C9NR09926C.

45. L. Li, F. Zhang, J. Wang, et al., "Achieving EQE of 16,700% in P3HT:$PC_{71}BM$ Based Photodetectors by Trap-Assisted Photomultiplication," *Scientific Reports* 5 (2015): 9181.

46. S. Gielen, C. Kaiser, F. Verstraeten, et al., "Intrinsic Detectivity Limits of Organic Near-Infrared Photodetectors," *Advanced Materials* 32 (2020): 2003818, https://doi.org/10.1002/adma.202003818.

47. A. Sharma, S. Singh, X. Song, et al., "A Nonionic Alcohol Soluble Polymer Cathode Interlayer Enables Efficient Organic and Perovskite Solar Cells," *Chemistry of Materials* 33 (2021): 8602–8611, https://doi.org/10.1021/acs.chemmater.1c01430.

48. J. Bertrandie, J. Han, C. S. P. De Castro, et al., "The Energy Level Conundrum of Organic Semiconductors in Solar Cells," *Advanced Materials* 34 (2022): 2202575, https://doi.org/10.1002/adma.202202575.

49. M. Houot, Z. Qiao, B. Hu, et al., "The Dynamics of Interfacial Trap States in High-Detectivity Near-Infrared Photomultiplication Organic Photodetectors," *Advanced Functional Materials* (2025): e18210, https://doi.org/10.1002/adfm.202518210.

50. D. Nodari, Z. Qiao, F. Furlan, O. J. Sandberg, K. Vandewal, and N. Gasparini, "Towards High and Reliable Specific Detectivity in Visible and Infrared Perovskite and Organic Photodiodes," *Nature Reviews Materials* 10 (2025): 842–856, https://doi.org/10.1038/s41578-025-00830-1.

51. P. D. Mannheimer, "The Light–Tissue Interaction of Pulse Oximetry," *Anesthesia & Analgesia* 105 (2007): S10–S17, https://doi.org/10.1213/01.ane.0000269522.84942.54.

52. Y. Khan, D. Han, A. Pierre, et al., "A Flexible Organic Reflectance Oximeter Array," *Proceedings of the National Academy of Sciences* 115 (2018): E11015—E11024, https://doi.org/10.1073/pnas.1813053115.

53. T. Yokota, T. Nakamura, H. Kato, et al., "A Conformable Imager for Biometric Authentication and Vital Sign Measurement," *Nature Electronics* 3 (2020): 113–121, https://doi.org/10.1038/s41928-019-0354-7.

54. H. Wang, W. Wang, J. J. Kim, et al., "An Optical-Based Multipoint 3-Axis Pressure Sensor with a Flexible Thin-Film Form," *Science Advances* 9 (2023), eadi2445, https://doi.org/10.1126/sciadv.adi2445.

55. T. J. Wijaya, S. Xiong, K. Sasaki, et al., "A Highly Stable Organic–Inorganic Hybrid Electron Transport Layer for Ultraflexible Organic Photodiodes," *Advanced Materials* 37 (2025): 2501951, https://doi.org/10.1002/adma.202501951.

56. K. Zuiderveld, "Contrast Limited Adaptive Histogram Equalization," in *Graphics Gems* (Elsevier, 1994), 474–485.

57. A. F. Frangi, W. J. Niessen, K. L. Vincken, and M. A. Viergever (1998), 130–137, https://link.springer.com/chapter/10.1007/bfb0056195.

58. N. Otsu, "A Threshold Selection Method from Gray-Level Histograms," *IEEE Transactions on Systems, Man, and Cybernetics* 9 (1979): 62–66, https://doi.org/10.1109/TSMC.1979.4310076.

59. K. BahadarKhan, A. A. Khaliq, and M. Shahid, "A Morphological Hessian Based Approach for Retinal Blood Vessels Segmentation and Denoising Using Region Based Otsu Thresholding," *PLoS One* 11 (2016): 0158996, https://doi.org/10.1371/journal.pone.0158996.

Supporting Information

Additional supporting information can be found online in the Supporting Information section.

Supporting File: aenm70745-sup-0001-SuppMat.docx.